

VORTEX WAKE INVESTIGATION BEHIND A WING-FLAP MODEL WITH JET SIMULATION

L.L.M. Veldhuis, R. de Kat
 *Delft University of Technology

Keywords: *Vortex wakes, jets, vortex modeling*

Abstract

To get a better insight in the effect of jets on vortex development and decay, stereo-PIV measurements were performed in a towing tank behind a flapped aircraft model. The experimental data set yields the wake vortex behavior in a range that extends from the vortex formation stage up to the mid-field (approximately $t^* = 2$ corresponding to 100 wingspans for $\alpha = 0^\circ$ and 60 wingspans for $\alpha = 6^\circ$). Although the jet does not affect the overall circulation strength, it has a significant effect on the velocity distribution in the wake. A new Double Gaussian vortex model is introduced that perfectly fits the measurement data.

Nomenclature

b	wing span [m]
b_0	initial vortex spacing [m]
c	wing chord [m]
C_L	lift coefficient [–]
C_l	rolling moment coefficient [–]
r	radial coordinate in cylindrical system [m]
S	surface area [m ²]
t_0	reference time ($= 2\pi b_0^2 / \Gamma_0$)
t^*	dimensionless time ($= t / t_0$)
T	thrust [N]
V	flow speed [m/s]
V_{tow}	towing speed [m/s]
V_θ	Tangential velocity component [m/s]
x	streamwise coordinate [m]
α	angle of attack [°]
δ_f	flap angle [°]

θ	azimuth angle in cylindrical system [°]
ν	kinematic viscosity [m ² /s]
Γ	circulation [m ² /s]
ω	axial vorticity [m/s ²]

Subscripts

0	initial
f	flap end
t	tip

Abbreviations

DUT	Delft University of Technology
TFOV	Traversing field of view

1 Introduction

To arrive at better predictions of vortex development and decay of wakes generated by large aircraft, extended numerical and experimental research programs are being performed by many researchers [1]. Apart from detailed investigations of vortex structure and characteristics in quasi-2 dimensional tests the analysis of vortices in a spatial and temporal mode is of primary importance for vortex wake encounter research. The presence of jet flow is known to have a significant influence on the structure of a vortex when the distance between the jet and the vortex is very small ([2, 3, 4, 6, 7, 8]). However, to date the analysis of this interaction problem was limited to numerical studies using simplified vortex and jet geometries [9, 10, 8, 4]. Moreover most experimental research of jet-vortex interaction has been done only at close distance behind the air-

craft due to the limited length of the windtunnels applied. A very interesting contribution has been given by Margaritis et al [5] who performed measurements on 4-vortex system in a windtunnel. Their jet-vortex distance is rather large compared to the current research but noticeable effect on the velocity distribution was found.

The current research, which was performed within the EU sponsored FARWAKE project, is focused to experimentally analyze the effect of jets on the development and decay of the vortices produced by a wing with flaps deployed, as typically found during take-off and landing [11]. For this purpose wake vortex flow experiments are performed behind a generic aircraft model using the Stereo-PIV measurement technique in a towing tank. According to the authors this experimental campaign on jet-vortex interaction is the first ever performed in a towing tank producing data at large distances behind the wake generating aircraft model.

2 Experimental setup

2.1 Towing Tank

The measurements were performed in the Delft University Towing Tank of the Ship Hydrodynamics Laboratory that is part of the Faculty of Mechanical, Maritime and Materials Engineering. The tank has a length of $142m$, a width of $4.22m$ and a nominal water depth of $2.5m$. For the present experiments the water depth was $2.30m$. The carriage, which holds the model, has a maximum speed of $7.5m \pm 0.01m/s$ but for the current research a lower speed of $3m/s$ was used. The tank dimensions along with the model position are presented in Fig. 1

2.2 Model

The wake generating model consists of a simple wing-flap model that can be equipped with water jets to simulate propulsion effects. This model is an exact copy of the SWIM model, that was used during earlier wind tunnel tests [14] and numerical investigations [13, 9](Fig. 2). The wing ($b = 0.60m$) is made of corrosion restrictive steel

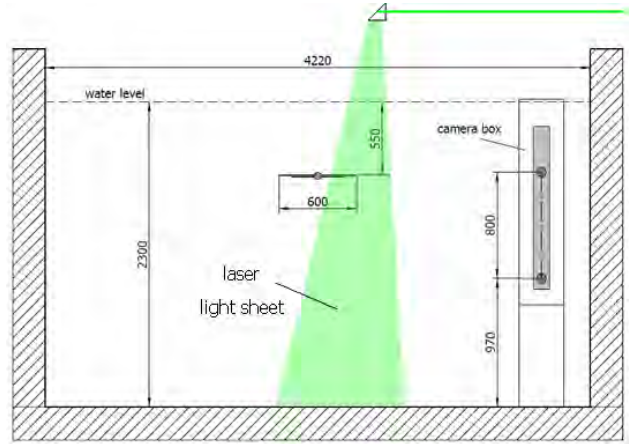


Fig. 1 Dimensions of the towing tank (a) and position of the SWIM-J model (dimensions in mm). The laser light sheet is introduced from the top.

and all other parts are made of aluminum alloy. To generate a typical vortex field, characteristic for the landing configuration of an aircraft, the model has fixed $2/3$ span flaps with a (fixed) flap angle of $\delta_f = 20^\circ$. A sketch of the model posi-

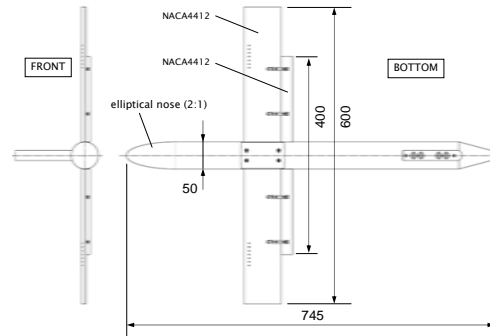


Fig. 2 Main characteristics of the SWIM-J model.

tioned in the towing tank is given in Fig. 3 and the main model characteristics are summarized in Table 1. The water waves created by the strut were very weak. Hence no detrimental effects on the trailing vortex flow pattern are present [15].

To simulate thrust effects removable jets ($diameter = 2cm$) were positioned at different positions in front of the outer flap ends (Fig. 4).

The jet velocity ratio, V_{jet}/V_∞ was close to 1.7. This velocity ratio is typical for the case of a landing aircraft.

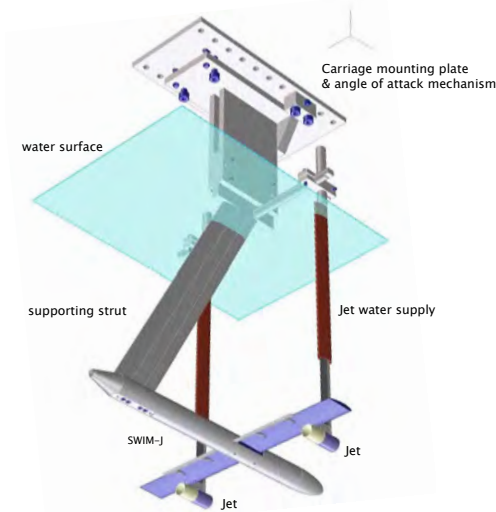


Fig. 3 Perspective sketch of SWIM-J mounted in the towing tank.

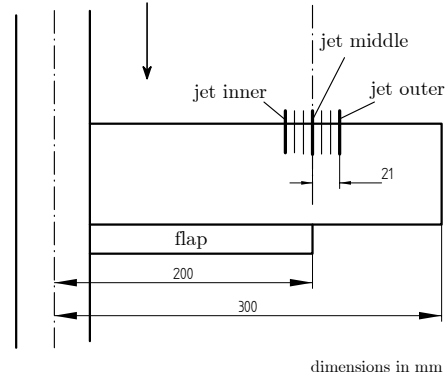


Fig. 4 Positions of the jets in front of the flap end.

2.3 Stereo-PIV setup

The PIV-system consisted of a two sensitive, double-frame, PIV cameras (5 Hz acquisition frequency, 1376 x 1040 pixels resolution, 12 bits), separated 55 cm in vertical direction. The lower camera was oriented horizontally, while the upper camera was inclined by 26° with respect to the horizontal. The light source was a double-cavity pulsed Nd:YAG laser (200 mJ pulse energy, 7 ns pulse duration). The light sheet was introduced vertically into the water through a partially submerged PLEXIGLAS window (Fig. 1). To be able to track the descending vortex system during the measurement run the traversing field of view technique (TFOV) [15] was applied. A sealed camera box equipped with an internal rail was utilized to translate the cameras in vertical direction. The camera traversing speed was selected to keep the tip and flap end vortex inside the field of view during 80 cm of vortex descent.

The distance of the camera from the measurement plane was about 1.4 m in the streamwise direction and about 0.5 m in spanwise direction resulting in an off-axis view of approximately 20° ("Scheimpflug" condition) and a FOV of 0.21 (H) x 0.31 (W) m². Images (double frames) were recorded with a fixed recording rate of 5 Hz. The time separation was limited by the large velocity gradients in the vortex core and yielded a maximum particle displacement of 6 pixels after merge (pre-merge maximum particle displacement 9 pixels). Typical runs recorded the vortex

Table 1 Geometrical data of the SWIM-J model.

Parameter	Value
Fuselage	
Length	0.600 m
Diameter	0.055 m
Nose geometry	2:1 elliptical
Wing	
Airfoil	NACA 4412
incidence angle	0°
Span	0.600 m
Taper ratio	1.0
Wing area	0.0450 m ²
Aspect Ratio	8.0
MAC	0.075 m
Flaps	
Flap span	0.40 m
Deflection angle	20°
Gap	1.9 mm
Overlap	0.8 mm
Flap chord	25 mm

evolution over 14 s to 25 s corresponding with 70 to 125 images.

The seeding mixture consisted of VESTOSYNT[®] particles of 56 μm diameter, diluted in water.

All images were analyzed with the PIV software package DAVIS 7 [16] resulting in a full 3 component velocity distribution in the measurement plane [17]. Since the complete velocity vector is obtained, perspective errors resulting from off-axis viewing are eliminated. In the analysis a 16×16 correlation window size was adopted with 50% overlap between consecutive windows, yielding 188×132 vectors per recording. The vector spacing is 1.6 mm. The typical error (RMS) of the correlations is 2.3 cm/s (0.140 pixel displacement) based on undisturbed flow measurements.

2.4 Test conditions

Separate runs were performed for 3 different configurations: a) no jets (denoted "no jet"), b) jets installed but inactive (denoted "jet off"), c) jets installed and active (denoted "jet on"). All tests were performed at a towing speed of 3 m/s equivalent to chord Reynolds number of 225.000 and Vortex Reynolds, Re_{Γ} , numbers of 150.000 and 220.000.

The angles of attack selected for the test was based on wind tunnel data available from earlier wind tunnel tests performed by de Bruin et al [14]. For comparison purposes, an extensive set of both wind tunnel data [14] and CFD data [13, 9] is available for the angles of $\alpha = 0^\circ$ and $\alpha = 6^\circ$ used in this survey. The lift coefficients for these angles are 1.0 and 1.6 respectively. Both angles of attack are in the linear range to prevent unwanted vortex decay effects due to flow separation over the wing surface.

During the tests the water temperature was approximately 15°C.

Because the vortex roll-up and decay process is highly dynamical the measured vortex parameters show statistical scatter. Therefore several runs per flow condition were performed to investigate the repeatability of the results. The coordi-

nate system is defined in Fig.5. All vector, velocity and vorticity plots are in the $y-z$ plane. The time dependence is directly correlated with the x displacement, as x increases in time with the towing velocity.

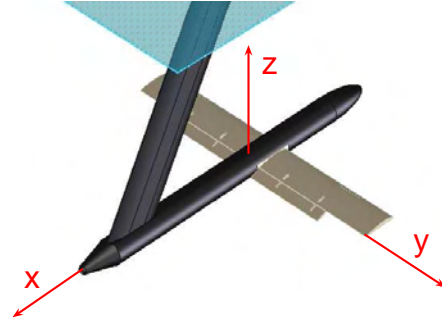


Fig. 5 Definition of the coordinate axes as used in this report.

3 DG vortex model

For detailed analysis of experimental data it is attractive to fit the scattered data with a velocity profile function. For this purpose various vortex models are available [18].

The Rankine model is a simplified model where viscosity is neglected whereas the models hence it fails in the description of the viscosity dominated flow that is encountered during vortex decay. Other models like the model proposed by Winkelmann and Burnham-Hallock [18] are based on empirical data that enable a reasonable fit for particular vortex profiles. Fabre and Jacquin [19] discuss a two radii model that is based on the analysis of experimentally found velocity data. This so-called VM2 model fits some data sets particularly well but lacks the time dependency effect due to the absence of a viscosity related term. The well known Lamb-Oseen vortex, that was derived on a theoretical basis already some 90 years ago, has been used extensively during the past decades. Since it forms an exact solution of the Navier-Stokes solution for laminar flow and shows the temporal development of the vortex it is a very attractive solution to be used in stability analysis of vortex systems

as encountered in a VWE-analysis. However, initial fitting of the velocity data obtained during the towing tank measurements led to unexpectedly poor results. Either the outer flow or the flow close to the vortex core could not match the measured data points but an overall acceptable fit was impossible. Therefore a new vortex model was tried out based on a solution of the linearized vorticity equation in cylindrical coordinates (x, r, θ) :

$$\frac{\partial V_\theta}{\partial t} = -v \frac{1}{r^2} \left(\frac{\partial(rV_\theta)}{\partial r} \right) + v \frac{1}{r} \frac{\partial^2(rV_\theta)}{\partial r^2} \quad (1)$$

Eq. 1 follows directly from the momentum equation in θ assuming an axi-symmetrical vortex field (i.e. $\frac{\partial(\cdot)}{\partial \theta} = 0$; $\frac{\partial(\cdot)}{\partial x} = 0$; $V_r = 0$). Hence, the velocity in circumferential direction is only a function of r and θ , $V_\theta = f(r, \theta)$. The boundary conditions for eq. 1 are:

$$V_\theta(r = 0, t) = 0 \quad (2)$$

$$V_\theta(r \rightarrow \infty, t) \approx \frac{\Gamma}{2\pi r} \quad (3)$$

$$V_\theta(r, t = 0) = \frac{\Gamma}{2\pi r} \quad (4)$$

Two basic vortex profiles that exactly fulfill these criteria are the well known Taylor vortex and the Lamb-Oseen vortex. The latter is given by the velocity distribution (applicable to laminar flow):

$$V_\theta(r) = \frac{\Gamma}{2\pi r} \left(1 - e^{-\frac{r^2}{\sigma^2}} \right) \quad (5)$$

which produces a Gaussian vorticity distribution:

$$\omega = \frac{\Gamma}{4\pi v t} e^{-\frac{r^2}{\sigma^2}} \quad (6)$$

The Lamb-Oseen vortex model is based on a single viscous core. Its time dependency has made it very attractive to describe the development and decay of typical vortex system found in many applications. In this case σ is the dispersion radius given by $\sigma = \sqrt{4vt}$. Squire introduced an effective turbulent viscosity that is likely to express more closely the turbulence associated with the flow directly outside the viscous core. He also

introduced a constant c to take into account a finite vortex core that exists directly after initiation by setting $\sigma = \sqrt{4vt + c}$.

In many cases, the vortex development process is less smooth than is anticipated by the simple V_θ -description as given by eq. 5. In general a tip vortex core starts to grow directly at the tip followed by entrainment from outer spread vorticity layers coming from the wing wake. The vorticity data that were found indeed show that the neighborhood of the tip contains blobs of vorticity that are gradually merging with the already formed initial vortex. In practice this means that a single Gaussian description of the vorticity distribution of eq. 6 may not be very accurate. This is especially the case when two vortices of comparable strength merge as is found during our tests with the tip and flap end vortex. In fact in this research double peak vorticity distributions have been found that can not be described with the single Gaussian Lamb-Oseen vortex model.

A practical solution to obtain a better fit of the experimental data, that supports the entrainment of outer vorticity, is the definition of a Double-Gaussian (DG) vortex model. This superposition of two Gaussian profiles is again an exact solution of eq. 1 which means that it has practical relevance and is expected to be found in physical flows. The velocity distribution of the proposed DG-model can be expressed as:

$$V_\theta(r) = \frac{\Gamma}{2\pi r} \left(b \left(1 - e^{-\frac{r^2}{\sigma_1^2}} \right) + (1 - b) \left(1 - e^{-\frac{r^2}{\sigma_2^2}} \right) \right) \quad (7)$$

Here the parameters σ_1 and σ_2 are the inner and outer vortex dispersion radii respectively, given by: $\sigma_i = \sqrt{4vt + c_i}$. Veldhuis and de Kat [11] show that in the case of two merging vortices indeed double peak velocity distributions are found that can only be accurately fitted with the DG-model. Although the empirical VM2-model of Jacquin [19], which is also based on a 2-radii model, comes reasonably close it fails to support the solution of the NS-equations and lacks a temporal vortex decay mechanism. With the success found during the initial application of the

new DG-model all PIV-data were fitted with this model in the subsequent analyzes. Fig. 6 gives an example of the typical difference between the tangential velocity data fit from the LO- and the DG-model.

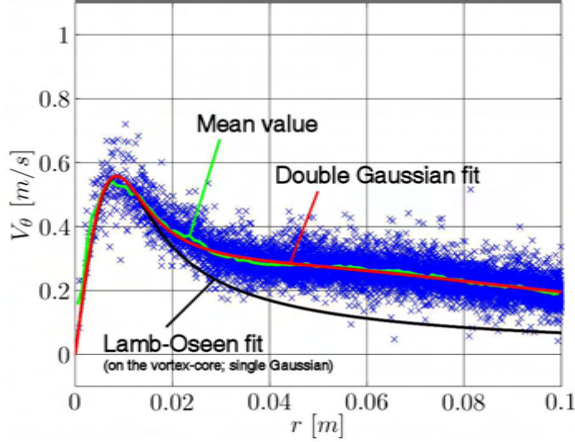


Fig. 6 Example of tangential velocity fit with the Lamb-Oseen and the DG-model. The scattered velocity data were obtained through multiple cross-cuts ($\theta = \text{constant}$) through the core.

4 Results

4.1 Wake parameters

Velocity profiles The velocity profiles are determined with respect to the vortex centre which was located with a dedicated core finding routines that is based on the vorticity distribution [11]. The tangential velocity profiles around the vortex core are determined from the $W - y$ and $V - z$ velocity profiles through the core. The profiles are fitted with the new Double Gaussian (DG) vortex model. The definition of the (crosswise) peak velocity requires special attention as in this investigation the DG-vortex model produces a fit with 2 peaks for approximately $\frac{1}{4}$ of the data. The double peaks that were found in the data are expected to be the result of 3-dimensional effects during the merge of the flap end and tip end vortex where the vorticity sheet from one vortex orbits the other. To provide additional information about the form of the velocity profiles (single versus double peak and peaky

versus flat distribution) the peak values as well as the 80% peak values are presented where appropriate.

Vorticity and circulation The vorticity needed for the calculation of the circulation is derived from the velocity field by using a 1st order central difference scheme. The peak vorticity (ω_{max}) is found from the DG fit equation.

The circulation is calculated from the surface integral of the vorticity:

$$\Gamma = \iint_S \omega dS \quad (8)$$

Or in discrete form:

$$\Gamma = \sum_S \omega_i s_i \quad (9)$$

where S indicates a summation over all the values that lie inside a circle with a radius of 10 cm from the vortex location. The circulation pre-merge is taken as the sum of 2 surface integrals over a circle of 5 cm radius from each vortex location. For comparison purposes, the circulation found by the fit over a circle of 10 cm is also calculated.

5 Results

The discussion on the results, described in the following paragraphs, is limited to 4 main cases:

- configuration 1: $\alpha = 0^\circ$, no jet
- configuration 6: $\alpha = 0^\circ$, jet on middle (referred to as jet on)
- configuration 8: $\alpha = 6^\circ$, no jet
- configuration 13: $\alpha = 6^\circ$, jet on middle (referred to as jet on)

The other cases are used to check the influence of the jet simulator supports and the location of the jets. Apparently these influences are very small [11]. Table 2 contains an overview of the main test characteristics.

5.1 Jet flow parameters

As described earlier, the jet velocity ratio, V_{jet}/V_{tow} was selected to be around 1.7 which more or less resembles the condition found during landing. The jet momentum coefficient can be defined as:

$$c_{\mu} = \frac{\rho_w V_{jet}^2 S_{jet}}{\frac{1}{2} \rho_w V_{tow}^2 S_{ref}} \quad (10)$$

Under present conditions $c_{\mu} = 0.113$, which is a rather low value. However, higher values of the jet velocity ratio were not possible due to limitations in the jet pumping capacity. For comparison with other jet vortex interaction studies it is beneficial to present the action of the jet in the form of a non-dimensional parameter [20] (see Table 2):

$$R_j = \frac{T}{\rho(k\Gamma_0)^2} \quad (11)$$

Here T is the thrust force per jet, Γ_0 is the root bound circulation value, in case of an equivalent elliptical lift distribution, and k represents a relaxation factor which gives the circulation strength of the vortex at the location where the jet and the vortex interact. In our case it is acceptable to assume $k = 1$ as the jet simulators are directly in front of the flap end vortex. In fact R_j is a measure for the ratio between the thrust force and the induced drag since $C_L \propto \Gamma_0$ and $C_{D_i} \propto C_L^2$, which means that $C_{D_i} \propto \Gamma_0^2$. The parameter R acts as a reference parameter to express the relative strength of the jet flow compared to the vorticity strength. As such the parameter $k\Gamma_0$, that approximates the circulation strength is an acceptable parameter. The jet characteristics were measured separately without the presence of co-flow. It was found that the jet is turbulent and it develops very fast in streamwise direction, as expected. From the PIV data the peak and average jet velocity were found to be: $V_{j_{peak}} = 5.1 \text{ m/s}$ and $\bar{V}_j = 4.8 \text{ m/s}$. Hence the actual jet velocity ratio is expected to be approximately 1.6, which is somewhat lower than the design value of 1.7.

Table 2 Main test characteristics.

Parameter	Value (range)
α	0° and 6°
C_L	1.0 at 0° a.o.a. 1.6 at 6° a.o.a.
V_{tow}	3 m/s
V_{water}	$1.141 \times 10^{-6} \text{ m}^2/\text{s}$
Γ_0	$0.143 \text{ m}^2/\text{s}$ at 0° a.o.a. $0.230 \text{ m}^2/\text{s}$ at 6° a.o.a.
Γ_{fe}/Γ_{tip} (approx.)	2 at 0° a.o.a. 1 at 6° a.o.a.
Re_c	1.97×10^5
Re_Γ	1.26×10^5 at 0° a.o.a. 1.88×10^5 at 6° a.o.a.
$(V_{jet})_{max}$	5.1 m/s
\bar{V}_{jet}	4.8 m/s
\bar{V}_{jet}/V_{tow}	1.60
t^*	0.02 to 2.2 at 0° a.o.a. 0.03 to 1.8 at 6° a.o.a.
x/b	1 to 110 at 0° a.o.a. 1 to 60 at 6° a.o.a.
R_j	0.133 at 0° a.o.a. 0.059 at 6° a.o.a.
Δ_j/b	-0.035, 0.000, +0.035

5.2 Velocity profiles

For the velocity profiles we focus on the post-merge range. In this range there is a stable counter rotating vortex pair. Fig. 7 shows typical velocity profiles for the 4 main flow cases. If we take a look at the cases for $\alpha = 0^\circ$ we see that the profile for *no jet* gives a clear peak. The profile for *jet on* shows a flattened peak (Figs. 7(a),(b)). The cases for $\alpha = 6^\circ$ show a plateau (or double peaked) profile for *no jet* and a peak profile for *jet on* (Figs. 7(c),(d)).

So for $\alpha = 0^\circ$ the jet has the effect flattens the peaky profile, while for $\alpha = 6^\circ$ the jet has the effect of generating a more peaky profile. Apparently the effect of the jet changes with angle of attack. This is an unexpected results since one would expect that the action of the jet always leads to a diffused flap end vortex that exhibits a "smeared out" flattened velocity distribution. An explanation for these velocity distributions is discussed in the next section. The temporal accuracy of the DG-model was checked, with the fit coefficients established at $x/b = 20$ for $\alpha = 0^\circ$ and $x/b = 15$ for $\alpha = 6^\circ$. The results showed any an 95 %accuracy of the fitted data compared to the experimental values.

5.3 Vortex merging

The final vortex is governed by the merging of the wing tip and flap end vortices. Here we will discuss the merging process for the 4 main cases in detail.

For the first case $\alpha = 0^\circ$, *no jet*, the first 16 vorticity intensity plots are shown in Fig. 8. In the first plot we see 2 distinct peaks of clockwise vorticity from the wing tip and flap end. Some small scale clockwise and anti-clockwise scatter can be seen as well, caused by the wing wake vorticity sheet. Until $x/b \approx 10$ the flap end and wing tip vortex just circle around each other. Beyond $x/b \approx 11$ the wing tip vortex starts to decrease in strength and it is subsequently wrapped around the flap end vortex to form 1 vortex at larger distance behind the wing.

For the second case, $\alpha = 0^\circ$, *jet on*, the first

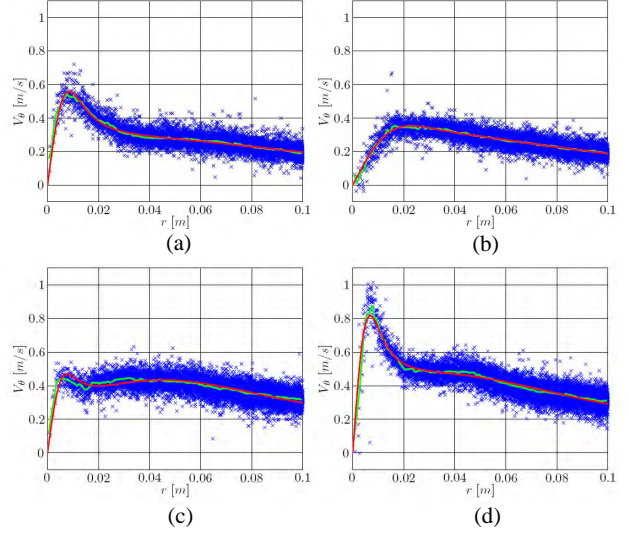


Fig. 7 Typical velocity fit profiles and measured velocity data for $t^* \approx 0.73$ for run 1 of: (a) $\alpha = 0^\circ$, *no jet* ($x/b \approx 36$) (b) $\alpha = 0^\circ$, *jet on* ($x/b \approx 36$) (c) $\alpha = 6^\circ$, *no jet* ($x/b \approx 22$) (d) $\alpha = 6^\circ$, *jet on* ($x/b \approx 22$)

16 vorticity intensity plots are shown in Fig. 9. In the first plot we see 1 distinct peak of clockwise vorticity from the wing tip and a vorticity region behind the flap end. Until $x/b \approx 11$ the flap end and wing tip vortex again show orbital movement. From $x/b \approx 11$ on, the vortices start to decrease in strength and merge with each other to form 1 vortex.

For the third case $\alpha = 6^\circ$, *no jet*, the first 12 vorticity intensity plots are shown in Fig. 10. In the first plot we see 2 distinct peaks of clockwise vorticity from the wing tip and flap end. Until $x/b \approx 10$ the flap end and wing tip vortex show orbital movement. Further downstream the vortices start to decrease in strength and the tip vortex is wrapped around the flap end vortex to form 1 vortex.

For the last case $\alpha = 6^\circ$, *no jet*, again the first 12 vorticity intensity plots are shown in Fig. 11. In the first plot we see 1 distinct peak of clockwise vorticity from the wing tip and a distributed vorticity region behind flap end due to the action of the jet. Almost immediately the flap end vortex starts to decrease in strength and is subsequently

wrapped around the wing tip vortex.

These findings are different from the ones found for a single pair of vortices shed from a wing. For a single pair of vortices it was found that, despite a different initial vorticity distribution and a quite different development of the vortex wake in the early stage, the final vortex pair structure at the end of the mid field was the same. This phenomenon was described earlier by Ciffone & Orloff [21] who found the same vortex structure at about 100-150 spans behind three different wing shapes (rectangular, diamond and swept) even though the initial vortex field showed completely different structure. This behavior was confirmed by Veldhuis et al [15] who performed PIV measurements behind an Airbus A340 model at different angles of attack.

The merging process of a double vortex pair is apparently dominated by a combination of the relative circulation strength of the tip and flap end vortices and the vorticity distribution, as the final circulation of the vortices is hardly changed by the action of the jet.

Fig. 12 was obtained through an interpolation of measured vorticity distribution. This figure shows that the vortex merging is promoted and the location moves upstream due to the jet. Summarizing we may state that the jet influences the flap end vortex vorticity distribution which in turn changes the merging process. The way this merging is influenced is determined by the relative vortex strength of the tip and flap end vortex. The merging process finally dictates the velocity distribution produced by the fully developed vortex pair.

5.4 Core radius

In Fig. 13 the development of the radii for the 4 main cases are shown versus t^* and x/b . The case for $\alpha = 0^\circ$, *no jet*, gives a slowly increasing vortex core radius with a wide peak (given by the 80% and 90%lines). When the jet becomes active, in the $\alpha = 0^\circ$ case, more noisy data is found and a larger core radius is produced that increases faster than the *no jet* case. The dashed lines show

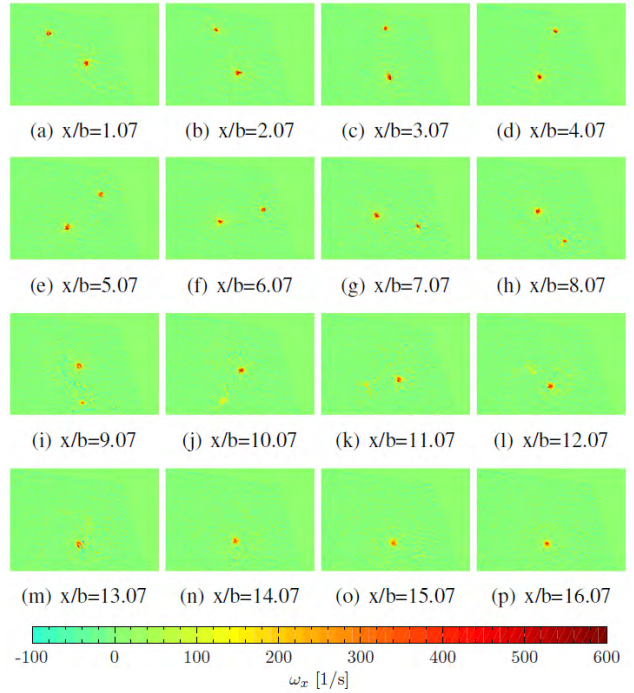


Fig. 8 Vorticity intensity distributions for $\alpha = 0^\circ$, *no jet*, run 7, t^* from ≈ 0.02 to ≈ 0.33 , x/b from ≈ 1.07 to ≈ 16.07

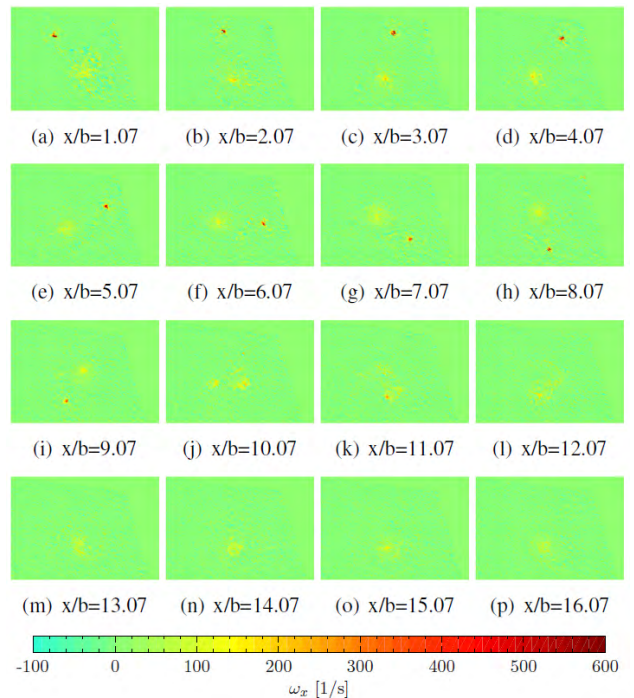


Fig. 9 Vorticity intensity distributions for $\alpha = 0^\circ$, *jet on*, run 6, t^* from ≈ 0.02 to ≈ 0.33 , x/b from ≈ 1.07 to ≈ 16.07

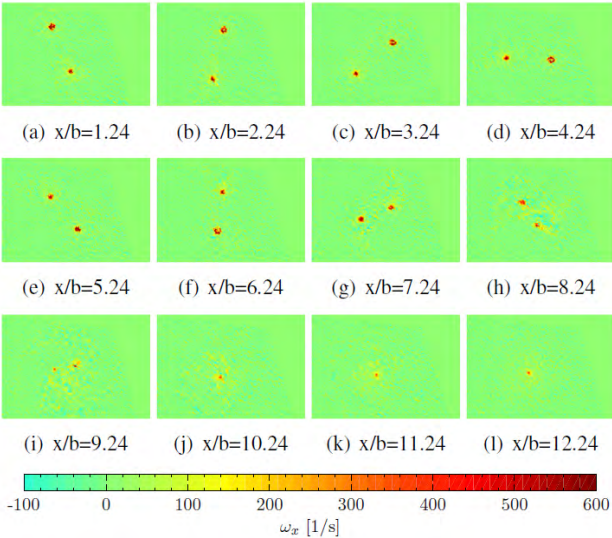


Fig. 10 Vorticity intensity distributions for $\alpha = 6^\circ$, *no jet*, run 4, t^* from ≈ 0.04 to ≈ 0.40 , x/b from ≈ 1.24 to ≈ 12.24

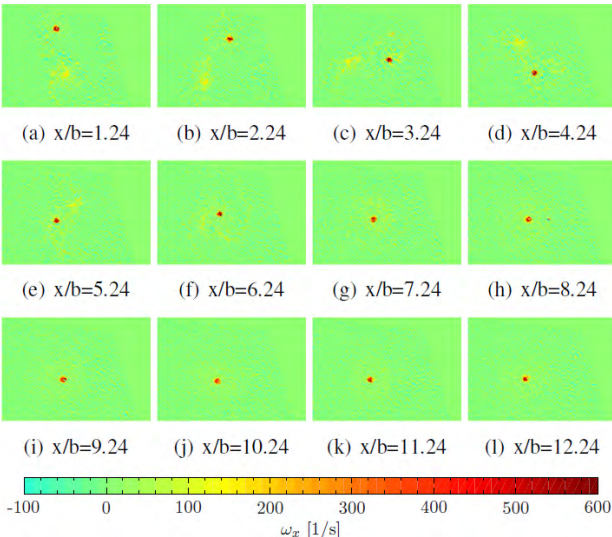


Fig. 11 Vorticity intensity distributions for $\alpha = 6^\circ$, *jet on*, run 4, t^* from ≈ 0.04 to ≈ 0.40 , x/b from ≈ 1.24 to ≈ 12.24

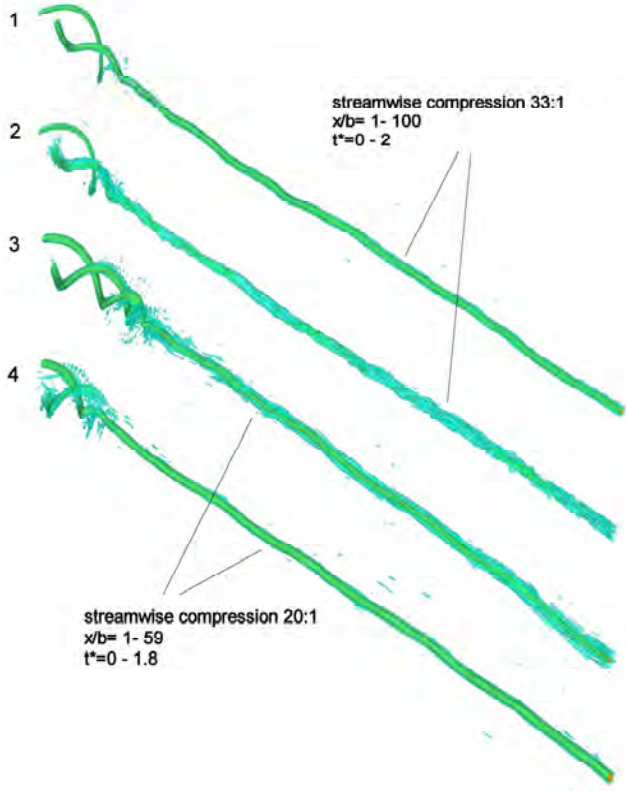


Fig. 12 Iso-surfaces of vorticity intensity; 1) $\alpha = 0^\circ$, *no jet*, 2) $\alpha = 0^\circ$, *jet on*, 3) $\alpha = 6^\circ$, *no jet*, 4) $\alpha = 6^\circ$, *jet on*, pictures are compressed in streamwise direction

that a wider peak is found (given by the 80% and 90% lines).

The case for $\alpha = 6^\circ$, *no jet*, shows a dramatic change with respect to the one obtained for $\alpha = 0^\circ$. Now an almost constant double peak/plateau vortex core radius is found with a small velocity peak value. The relative change in the circulation distribution between tip and flap end vortex apparently not only changes the final circulation strength but also has a major effect on the velocity distribution. Surprisingly the action of the jet in the $\alpha = 6^\circ$ case, again leads to a more peaky velocity distribution as can be seen from the slowly increasing vortex core radius with the 80% and 90% peak lines close together.

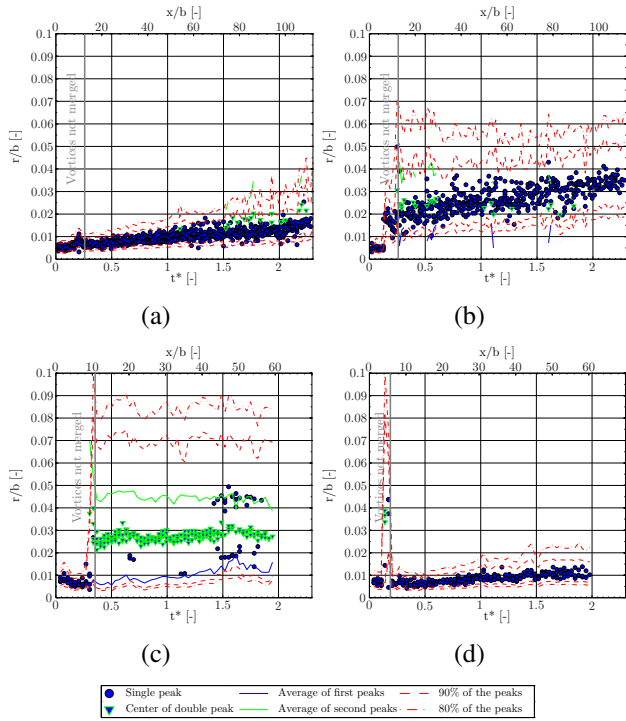


Fig. 13 Development of the vortex core radius for all runs for: (a) $\alpha = 0^\circ$, *no jet* (b) $\alpha = 0^\circ$, *jet on* (c) $\alpha = 6^\circ$, *no jet* (d) $\alpha = 6^\circ$, *jet on*

5.5 Circulation

For the circulation the theoretical values are $0.143m^2/s$ for $\alpha = 0^\circ$ and $0.230m^2/s$ for $\alpha = 6^\circ$ based on an elliptical wing loading distribution. In the experiments the circulation is determined

over a defined area as described in section 4.1. All cases start close to the theoretical value and decrease almost linearly. It must be noted that in the pre-merge phase the circulation is determined by adding the Γ_{5cm} values of the wing tip and the flap end vortices. This causes the peculiar behavior just before merge. The decrease in circulation is most likely caused by the diffusion out of the integration area of the vorticity. At the end of the runs of $\alpha = 6^\circ$ the sudden drop in circulation is caused by the vortex starting to leave the FOV.

For comparison purposes the fitted theoretical circulation of the DG-vortex model over an integration circle of $10cm$ is given as well (Fig. 15). Only the circulation based on the fit of the first vortex (the top one) is shown, thus the pre-merge values are likely to be false due to the fit error in this region. Note that the circulation found from the DG-fit shows the same behavior as the circulation given by the experimental data. The fitted data show a somewhat higher value which may be contributed to the limited observation area.

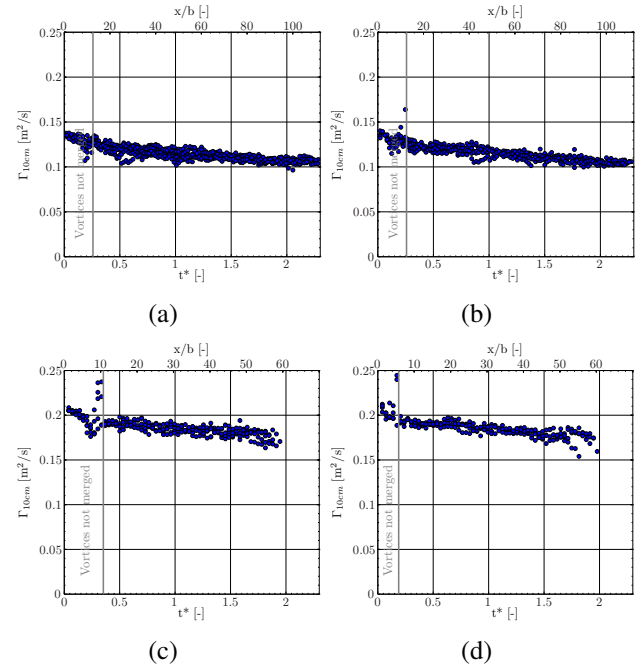


Fig. 14 Development of the circulation found from the surface integration procedure for all runs for: (a) $\alpha = 0^\circ$, *no jet* (b) $\alpha = 0^\circ$, *jet on* (c) $\alpha = 6^\circ$, *no jet* (d) $\alpha = 6^\circ$, *jet on*

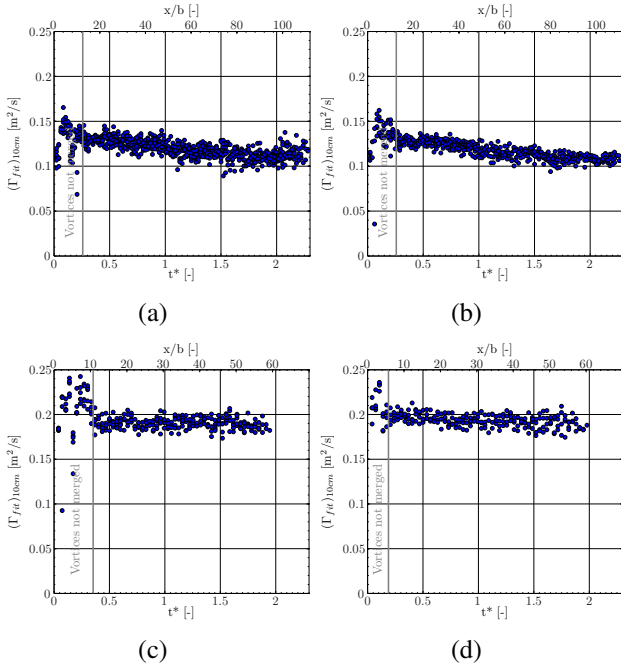


Fig. 15 Development of the circulation found from the fit procedure for all runs for: (a) $\alpha = 0^\circ$, no jet (b) $\alpha = 0^\circ$, jet on (c) $\alpha = 6^\circ$, no jet (d) $\alpha = 6^\circ$, jet on

5.6 Vortex trajectories

The vertical vortex trajectories are presented in 16 and 17. In general all figures show a good overlap of the different runs which demonstrates the good repeatability of the experiments. In all figures, at small distances behind the wing, the two separate wing tip and flap end vortices are identified depending on their location (via the core finding routine), indicated with different colors. These separate co-rotating vortices experience an orbital movement before the merging takes place. The spanwise position of the merged vortex is very close to the theoretical value of an elliptical loading distribution: $\frac{\pi}{4}b = 0.236m$. Comparing the sinking speed of the vortices (as calculated by taking a linear fit over the complete x/b -range in Fig. 16) we find approximately: $V_{sink} = 0.028m/s$ and $V_{sink} = 0.057m/s$ for the cases $\alpha = 0^\circ$ and $\alpha = 6^\circ$, respectively. Theoretical vortex models like: Biot-Savart, Lamb-Oseen, Rankine, Double Gaussian, etc., that are set up for a double infinite vortex pair, pro-

duce much higher values ($V_{sink} \approx 0.048m/s$ and $V_{sink} \approx 0.077m/s$). This can be explained by the fact that the downward speed is not constant, as can be seen in Fig. 16. This means that the approximation of a linear fit over the complete x/b -range underestimates the sinking speed. In fact, based on the data in Fig. 16 the downward motion of the vortex can be divided into 3 different parts, as sketched in Fig. 18. The first part (A) is completely dictated by the two separate tip and flap end vortices that finally lead to merging. Therefore, it is obvious that a simple vortex pair model for the complete wing is inappropriate in this range. In part (B) the merging is completed and the vortex pair model may lead to reasonable results. However, in our experiments we find a third region (C) where the descend speed seems to stabilize to a smaller value. No satisfactory explanation for this phenomenon has been found to date.

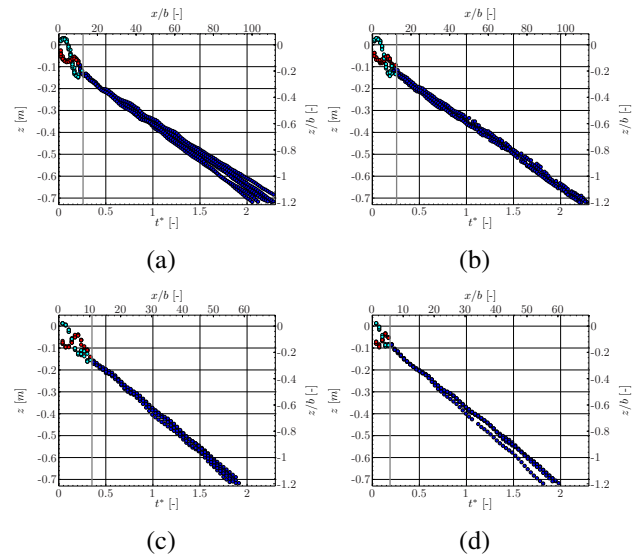


Fig. 16 Vertical location of the vortices for all runs for: (a) $\alpha = 0^\circ$, no jet (b) $\alpha = 0^\circ$, jet on (c) $\alpha = 6^\circ$, no jet (d) $\alpha = 6^\circ$, jet on

6 Rolling moment analysis

Many studies on vortex wake encounters have shown that the most important disturbance experienced by a follower aircraft is a rolling moment

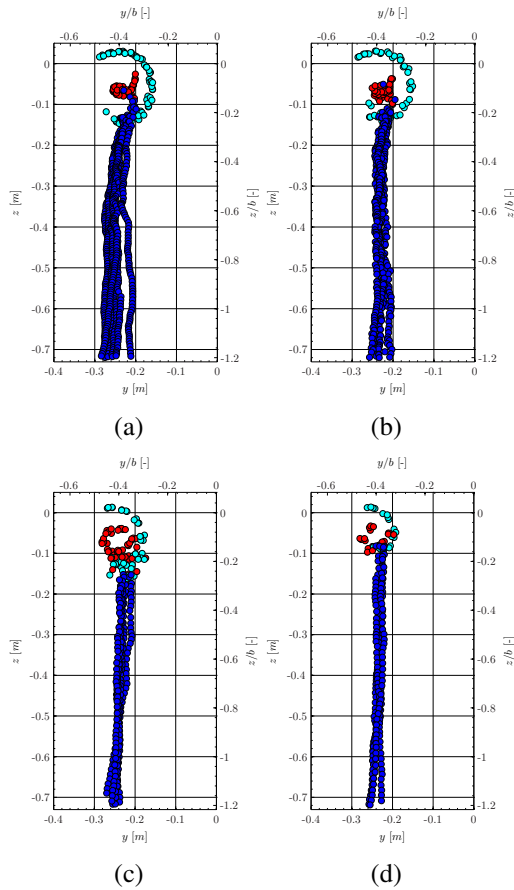


Fig. 17 Rear view of the location of the vortices for all runs for: (a) $\alpha = 0^\circ$, no jet (b) $\alpha = 0^\circ$, jet on (c) $\alpha = 6^\circ$, no jet (d) $\alpha = 6^\circ$, jet on

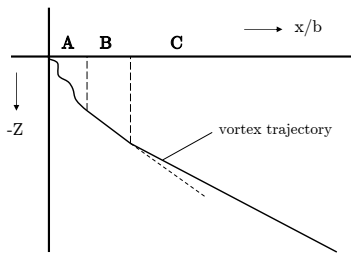


Fig. 18 Different domains (A), (B) and (C) found in all vortex displacement plots.

upset. Hence the induced rolling moment by any particular vortex system generated by a leader aircraft could be used to indicate the general danger of an VWE. The calculation of the rolling moment is hindered by the fact that its value strongly depends on aircraft and flight parameters like inertial coefficients, flight speed and altitude. Nevertheless a comparison of the effect of the various vortex models on the induced rolling moment compared to the rolling moment capability of typical aircraft may give us some insight in the relevance of the jet influence on the vortex velocity profiles. For this reason a simple aerodynamic model was developed which calculates the main wing aerodynamic characteristics of a follower aircraft based on a given input of leader aircraft data and different vortex models produced. The follower wing model is based on lifting surface approximation of the wing.

The effect of the different velocity distributions is found by simply changing the induced inflow angle at the location of the follower wing while maintaining a constant circulation strength of the leader aircraft. In case of the DG model, 4 different velocity distributions, as found from the experiment were analyzed (Fig. 19).

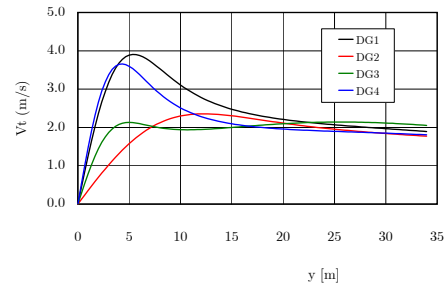


Fig. 19 Double Gaussian (DG) velocity distributions applied in the rolling moment analysis.

The DG-fits were taken at $x/b \approx 36$ for $\alpha = 0^\circ$ and $x/b \approx 22$ for $\alpha = 6^\circ$ while the absolute value of the tangential velocity was scaled with the fixed value of the circulation strength, Γ_v , of the leader vortex. The vortex core size was set to 7% of the leader aircraft span.

For comparison purposes 2 different (heavy) leader aircraft (Airbus A380 and Boeing B747) have been combined with a lighter follower air-

craft (Boeing B737). It should be clear that the calculated rolling moment coefficient, $C_l = l/\frac{1}{2}\rho V_\infty^2 S b$, only gives a rough indication of the true VWE-effect since pilot action as well as rolling moment relieve due to roll rate reaction of the follower aircraft were left out of the analysis.

The maximum induced rolling moment is experienced when the aircraft's wing center and the leader vortex center are exact aligned. Therefore in subsequent analyzes the calculations are restricted to the $Y_v = 0, Z_v = 0$ only.

It should be noted that the application of the experimentally found velocity distributions does not imply that they represent real flight conditions as the effect of atmospheric turbulence as well as leader aircraft flap deflection were not taken into account. The comparison is made only to signify the importance of the vortex merging process that is dictated by the combined influence of the tip vortex/flap vortex strength ratio, Γ_t/Γ_f , and the action of the jet (see section 5.3).

The models DG1 to DG4 are represented by the velocity distribution (fits) of the experiments according to the following flow cases:

- DG1 : $\alpha = 0^\circ$, *no jet*
- DG2 : $\alpha = 0^\circ$, *jet on*
- DG3 : $\alpha = 6^\circ$, *no jet*
- DG4 : $\alpha = 6^\circ$, *jet on*

The effect of the change in the merging process (through action of the jet) is presented in Fig. 20.

Going from the DG1-model to the DG2-model a noticeable reduction of C_l is found for both leader-follower combinations. The increase of C_l between models DG3 and DG4 expresses a detrimental jet-effect. However it proves that the application of a jet interacting with the flap end vortex apparently leads to rolling moment effects that may be tuned to obtain less dangerous trailing vortex fields. To quantify whether the effect of the different vortex models (and thus the jet effect) could be relevant for the case of the A380 in flight, the difference between B747 and A380 is

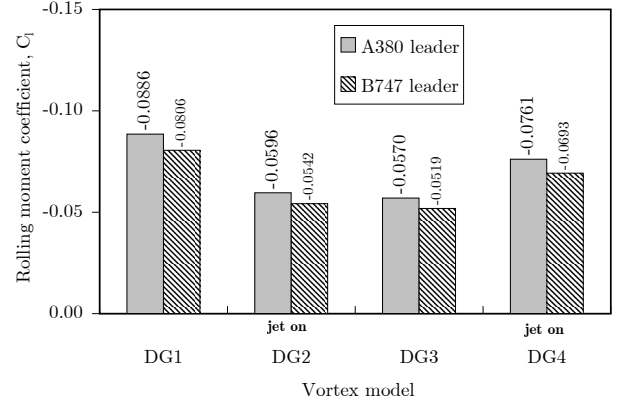


Fig. 20 Rolling Moment coefficient due to DG-model velocity distributions for a B747 and A380 leader and a B737 follower aircraft.

compared with the change is the rolling moment that may be obtained by applying jets through the a rolling moment ratio, *RMR*:

$$RMR = \frac{C_{l_{B747-follower}}}{C_{l_{A380-follower}}} \quad (12)$$

in comparison to the jet effect:

$$\Delta C_{l_{jet}} = \left| \frac{\{\Delta C_{l_{leader-follower}}\}_{jet\ on} - \{\Delta C_{l_{leader-follower}}\}_{no\ jet}}{\{\Delta C_{l_{leader-follower}}\}_{no\ jet}} \right| \quad (13)$$

In Table 3 and 4 the value of RMR and the vortex induced rolling moment for the B737 are given, respectively. From the value of RMR we see that for the same vortex model the A380 produces a 9% higher induced rolling moment than the B747. Of course this value is directly related to the initial circulation strength of both aircraft which are $\Gamma_v = 601.4 m^2/s$ and $\Gamma_v = 661.0 m^2/s$ for the B747 and A380 respectively.

If we take the average merging/jet effect of all 4 DG cases ($\overline{\Delta C_{l_{jet}}} = 0.02297$) and the average rolling moment coefficients ($\overline{C_l} = -0.06716$) to produce a ratio, we find the relative merging/jet effect to be 34%! Hence one could argue that by applying a well tuned vortex-jet interaction layout the induced rolling moment effect of the A380 could finally become smaller than the one produced by an unaltered B747 aircraft.

7 Conclusions

Stereo-PIV measurements behind a generic flapped wing model (SWIM-J) with jet simulators have been performed successfully in a towing tank. From this an extensive data set has been obtained representing the complete development of the vortex wake from the roll-up process, through vortex merging to the vortex pair in the mid to far field ($x/b \approx 100$).

To obtain accurate vortex related parameters like vortex core radius, velocity distribution, etc. a new Double-Gaussian (DG) vortex model was proposed that fits the experimental data exceptionally well. Both the raw data and the fitted data show that the jet effect on the effective circulation strength is limited but significant effects were found in the velocity distributions and related parameters (like the vortex core).

The main jet effect in the mid-field is caused by a change in the flap end vorticity distribution. The jet flow promotes the merging process between tip vortex and flap end vortex. The form of the final velocity distribution in the wake depends on this merging process that in turn is directly influenced by the circulation strength ratio of the tip and flap end vortex and the action of the jet.

A preliminary induced rolling moment analysis has been performed to obtain a rough estimate of the effect that the changed velocity distributions due to the jet may have. For this purpose combinations of two leader (A380 and B747) and one follower aircraft (B737) were analyzed. The data show that the merging/jet effect on the induced rolling moment is larger than the difference in the rolling moment caused by the A380 and B737 aircraft. Hence it may be concluded that the application of a well tuned jet effect (optimized position and jet velocity), may lead to reduced rolling moment upset for follower aircraft.

8 References

References

- [1] Gerz, T., Holzäpfel, F., Darracq, D., Commercial Aircraft Wake Vortices, Progress in

Table 3 Rolling Moment Ratio, *RMR*, as found for the B737 follower aircraft.

Follower: B737	
Vortex Model	RMR
DG1	0.90999
DG2	0.90997
DG3	0.90997
DG4	0.90998

Table 4 Vortex Merging/Jet effect on the rolling moment coefficient of a B737 follower aircraft.

Leader	Vortex Model	C_l	$ (\Delta C_l)_{jet} $
A380	DG1	-0.0806	0.0290
	DG2	-0.0542	
	DG3	-0.0519	0.0191
	DG4	-0.0693	
747	DG1	-0.0886	0.0264
	DG2	-0.0596	
	DG3	-0.0570	0.0174
	DG4	-0.0761	

- Aerospace Sciences Vol. 38, Pergamon Press, 2002
- [2] F. Garnier, C. Ferreira Gago and F. Utheza, Numerical simulation of large-scale structures in exhaust jet/wake vortex merging, AIAA-2001-1039
- [3] E. Coustols, E. Stumpf, L. Jacquin, F. Moens, H. Vollmers and T. Gerz, Minimised wake, a collaborative research programme, AIAA-2003-0938
- [4] R. Paoli, F. Laporte, B. Cuenot, and T. Poinso, Dynamics and mixing in jet/vortex interactions, *Physics of Fluids*, 15, 1843-1850, 2003.
- [5] P. Margaritis, D. Marles, I. Gursul, Experiments on jet/vortex interaction, *Experiments in Fluids* 44, 261-278, 2008
- [6] G. Huppertz, E. Fares, R. Abstiens and W. Schroder, Investigation of engine jet/wing-tip vortex interference, *Aerospace Science and Technology* 8 (2004) pp. 175-183.
- [7] L. Jacquin and P. Molton, Experiments on cold/hot jet-vortex interaction, FAR-WAKE Technical report TR 2.1.2-6, 2006
- [8] S. Brunet; F. Garnier and L. Jacquin, Numerical/ experimental simulation of exhaust jet mixing in wake vortex, AIAA-99-3418, 1999
- [9] W.A. Hageraats, Fluid dynamic simulations of vortex-jet interaction, MSc Thesis Report, Delft University of Technology, 2006
- [10] R. de Kat, Vortex decay behind a generic wing-flap-jet aircraft model, MSc Thesis Report, Delft University of Technology, 2007
- [11] L. Veldhuis and R. de Kat, Towing tank experiments of cold jet-vortex interaction on a generic wing-flap model, FAR-WAKE Technical report TR 2.2.1-5, 2006
- [12] A.C. de Bruin and G. Winckelmans, Cross-flow kinetic energy and core size growth at analytically defined wake vortex pairs, Report NLR-CR-2005-412, 2005
- [13] A. Benkenida, G. Jonville, and D. Darracq, Numerical study of wake vortices of a generic aircraft model, In 19th AIAA Applied Aerodynamics conference, Anaheim, USA, AIAA Paper 2001-2428.
- [14] A.C. de Bruin and F.L.A. Ganzevles, Data analysis of wake survey tests behind SWIM model geometry in DNW-LST and DNW-LLF wind tunnels, Report NLR-TR-2001-201, 2001
- [15] L.L.M. Veldhuis; F. Scarano and K. van Wijk, Vortex wake investigation of an Airbus A340 model using PIV in a towing tank, C-Wake Report, PR1.1.3-TUD, 2001
- [16] Anon., Manual LaVision DaVis v7.1.
- [17] A.K. Prasad, Stereoscopic particle image velocimetry, *Exp. Fluids* 29, pp 103-116, 2000
- [18] A.C. de Bruin and G. Winckelmans, Cross-flow kinetic energy and core size growth at analytically defined wake vortex pairs, Report NLR-CR-2005-412, 2005
- [19] D. Fabre and L. Jacquin, Short-wave cooperative instabilities in representative aircraft vortices, *Phys. Fluids* 16, 1366, 2004
- [20] A. de Bruin, Analysis of near wake data with and without simulated jets - Airbus-UK experiment from C-Wake project, FAR-WAKE Report D 2.1.1-1, 2006
- [21] D.L. Ciffone and K.L. Orloff, Far-field wake-vortex characteristics of wings, *J. Aircraft*, Vol. 12, No. 47, May 1975, pp. 464-470

8.1 Copyright Statement

The authors confirm that they, and/or their company or institution, hold copyright on all of the original material included in their paper. They also confirm they have obtained permission, from the copyright holder of any third party material included in their paper, to publish it as part of their paper. The authors grant full permission for the publication and distribution of their paper as part of the ICAS2008 proceedings or as individual off-prints from the proceedings.